On the Use of Ultrasound-Based Technology for Cargo Inspection

Yuri Álvarez-López
Área de Teoría de la Señal y Comunicaciones,
Universidad de Oviedo,
Edificio Polivalente,
Mod. 8, 8.1.02. Campus Universitario de Gijón,
Gijón 33203, Spain
e-mail: yalopez.tsc@gmail.com

José A. Martínez-Lorenzo[1]
Department of Mechanical and
Industrial Engineering,
Northeastern University,
211 Snell Engineering Center,
360 Huntington Avenue,
Boston, MA 02115
e-mail: j.martinez-lorenzo@neu.edu

A new guided wave imaging application for fast, low-cost ultrasound-based cargo scanning system is proposed. The ultimate goal is the detection of high-atomic-number, shielding containers used to diminish the radiological signature of nuclear threats. This ultrasonic technology has the potential to complement currently deployed X-ray-based radiographic systems, thus enhancing the probability of detecting nuclear threats. An array of ultrasonic transceivers can be attached to the metallic structure of the cargo to create a guided Lamb wave. Guided medium thickness and composition variation creates reflections whose placement can be revealed by means of an imaging algorithm. The knowledge of the reflection position provides information about the shielding metallic container location inside the cargo. Moreover, due to the low coupling between metallic and nonmetallic surfaces, only the footprint of metallic containers shows up in the imaging results, thus avoiding false positives from plastic or wooden assets. As imaging capabilities are degraded if working with dispersive Lamb wave modes, the operating frequency is tuned to provide a tradeoff between low dispersion and real-time image resolution. Reflected waves in the guided domain bounds may limit the performance of imaging methods for guided media. This contribution proposes a solution based on real-time Fourier domain analysis, where plane wave components can be filtered out, thus removing nondesired contributions from bounds. Several realistic examples, scaled due to limited calculation capabilities of the available computational resources, are presented in this work, showing the feasibility of the proposed method.
[DOI: 10.1115/1.4032724]

1 Introduction

Nonproliferation of nuclear threats has been identified as a critical objective in the war against nuclear terror. To ensure effective nonproliferation, it is critical to proactively identify the transport of commodities associated with illicit nuclear materials and nuclear weapons.

Radioactive atoms, typically characterized for having a high atomic Z-number, for example, plutonium ($Z = 94$) and uranium ($Z = 92$), are unstable and give off various types of radiations, including gamma rays and neutrons. Gamma-ray spectrum analysis and neutron detectors, based on helium-3 gas, can be used to detect these types of nuclear radioactive materials [1]. Unfortunately, the signatures of these radiological materials can be diminished by enclosing them in a container made of other nonradiological, high Z number materials, like lead ($Z = 82$), thus making its detection difficult.

Dual-energy radiography systems and X-ray back scattering can be successfully used to detect the shielding materials; and they are widely used in existing state-of-the-art cargo-inspection security portals [2]. However, this type of detection can be difficult in cargo environments cluttered by high-density materials. Furthermore, those high Z-number shielding containers can be concealed within the cargo structure as depicted in Fig. 1.

This contribution introduces the theoretical bases as well as the proof-of-concept for a fast, low-cost ultrasound imaging system, operating at 100 kHz, capable of detecting the footprint of metallic containers or concealed compartments within cargo boxes [3–5] as depicted in Fig. 2. If made of high Z-number material, these compartments can be used to conceal the radiologic response of nuclear threats. The proposed sensing technology aims to complement existing cargo screening systems (e.g., X-ray scanners) providing a complimentary noninvasive detection method.

For this purpose, an array of ultrasonic transceivers is attached to the metallic structure of the cargo to create a low-dispersive guided Lamb wave. Variation in the media composition and/or thickness creates reflections that can be detected in the images provided by an imaging algorithm.

The system is based on the assumption that cargo containers have a flat metallic base plate, so transducers can be placed at the sides of the plate for scanning, as depicted in Fig. 2. In practice, not all the cargo containers have a metallic base plate. Wooden floors can be found in some of them (truck and ship cargo containers mainly). Only those built for special goods (e.g., refrigerated containers) are fully made of steel or aluminum [3], sometimes consisting on welded metallic plates in the case of large containers. However, there are scenarios where single metallic base plate containers can be found quite often, e.g., air cargo [4,5] (Fig. 1). In particular, in the air cargo container specifications described in Ref. [5], it is stated "The base 1 is made of a material having a shear strength of at least 7300 psi (50 MPa). It may be made of an aluminum alloy sheet material which is preferably about 2.5 mm thick."

In order to validate the feasibility of the proposed ultrasound-based imaging system for cargo inspection, this contribution focuses on the evaluation of the imaging technique for different transmitting and receiving transceiver layouts, ranging from a full transmitting and receiving phased array to a single transmitter with few receiving positions. The goal is to prove that the method is capable of detecting the footprint of metallic objects in cargo. The imaging technique is mainly based on the well-known time reversal method, also known as "delay-and-sum," suitable for synthetic aperture and phased array systems [6–8,26]. A Fourier-based filtering for dealing with nondesired reflections is also tested, thus extending the two-dimensional (2D) validation based on acoustic waves presented in Ref. [9].

2 Ultrasound Imaging System Description

2.1 Background. Ultrasonic testing is used in a wide range of applications [10–16], for example, structural health-monitoring

[1]Corresponding author.

Contributed by the Noise Control and Acoustics Division of ASME for publication in the Journal of Vibration and Acoustics. Manuscript received July 3, 2015; final manuscript received January 18, 2016; published online April 7, 2016. Assoc. Editor: Nicole Kessissoglou.

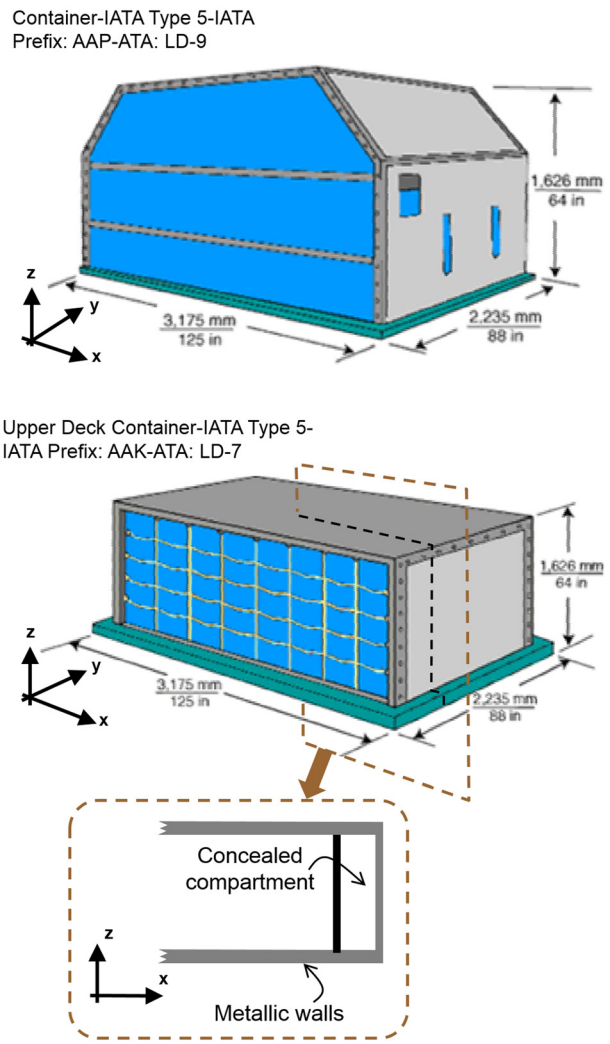

Fig. 1 Two examples of cargo containers with a metallic base plate, the second having a shielded camouflaged compartment that can be used for concealing goods or radioactive threats. Cargo schemes extracted from Ref. [4].

[10], aircraft inspection [15], and medical imaging [16]. Among the large amount of ultrasonic techniques, the use of guided waves [17,18] (e.g., Lamb waves [19–22]) has been found to be of interest in applications such as rail and pipe testing [11,12], weld inspection [13], or aircraft lap joints [14]. Guided wave imaging techniques have been developed for this purpose [6,7].

The imaging problem in guided wave structures becomes more challenging as the waveguide is bounded by reflecting interfaces. Optimal imaging needs to take into account all ultrasonic reflections of the wave from each possible scatterer. To overcome this limitation, a matched filter-based imaging method is proposed in Ref. [8], achieving high resolution images. The limitation is that the knowledge of the medium geometry is required.

Wave analysis in the wavenumber or Fourier domain has also been explored. The knowledge of the different modes propagating through the guided media [23] can be used to recover information about the location of cracks and media inhomogeneities, as proposed in Refs. [24,25].

As indicated in Ref. [8], reflected waves in the guided domain bounds may limit the performance of imaging methods for guided media. This contribution takes advantage of a solution based on a real-time Fourier domain analysis, where plane wave components can be filtered out, thus removing nondesired contributions from the geometry bounds.

2.2 Ultrasound Imaging Algorithm. The proposed ultrasonic imaging system has the setup depicted in Fig. 3. Several transmitters and receivers are placed along the x-axis for a fixed y-axis position, y_{obs}. Imaging domain points are denoted as (x', y'). Range is y-axis (depth) and cross-range is x-axis (aperture).

Imaging domain ultrasonic reflectivity, $\rho(x', y')$, can be estimated from the displacement recorded in the receivers, $U(x, y_{obs}, f)$ over a certain frequency bandwidth, B (spanning from 0 to f_{max}), by back-propagating the recorded displacement, adding them coherently [26]. For the case of a single evaluation point (x', y'), reflectivity is given by Eq. (1)

$$\rho(x', y') = \Sigma_x \Sigma_f U(x, y_{obs}, f) \exp(\mathbf{j}\, k_1 R_{obs}) \exp(\mathbf{j}\, k_1 R), \quad f = [0 : \Delta f : f_{max}] \tag{1}$$

where k_1 is the medium wavenumber, $k_1 = 2\pi f/c_1$, and c_1 is the excited Lamb mode velocity in the supporting medium (e.g., the metallic structure of the cargo).

R and R_{obs} are defined as

$$R = \left((x_{Tx} - x')^2 + (y_{Tx} - y')^2\right)^{1/2} \tag{2}$$

$$R_{obs} = \left((x - x')^2 + (y_{obs} - y')^2\right)^{1/2} \tag{3}$$

with (x_{Tx}, y_{Tx}) the position of the transmitter. Δf is the frequency sampling rate. If the displacement is recorded in a time interval t at every receiving position x, $u(x, y_{obs}, t)$ ranging from t_1 to t_2, in Δt time steps, then, the relationship between time and frequency is

$$f_{max} = 1/\Delta t \tag{4}$$

$$\Delta f = 1/(t_2 - t_1) \tag{5}$$

The displacement in the frequency domain, $U(x, y_{obs}, f)$, is calculated by simply taking the Fourier transform of the recorded displacement in the time domain, $u(x, y_{obs}, t)$

$$U(x, y_{obs}, f) = \Sigma_t u(x, y_{obs}, t) \exp(-\mathbf{j}\, 2\pi f t), \quad t = [t_1 : \Delta t : t_2] \tag{6}$$

The imaging system is proposed to be used in a guided medium, such as a metallic plate which thickness much smaller than its width and length. Reflections in waveguide sides create nondesired responses in the resulting image that degrade the system performance. To overcome this limitation, the observed displacement can be analyzed in the Fourier domain [27], filtering out nondesired plane wave contributions, as proposed in Ref. [24]. As y_{obs} is constant (i.e., the position of the aperture in the range axis), only the Fourier transform across x-axis (cross-range) needs to be calculated

$$U_k(y_{obs}, k_x, f) = \int_x U(x, y_{obs}, f) \exp(-\mathbf{j}\, k_x x) dx \tag{7}$$

k_x is the x-component of the k_1 wavenumber, ranging from $-\pi/\Delta x$ to $\pi/\Delta x$, where $\Delta x = x_2 - x_1$, is the sampling rate of the aperture (cross-range axis) [27]. The spectral resolution, Δk_x, is inversely proportional to the aperture size, L_{Rx}

$$\Delta k_x = 2\pi/L_{Rx} \tag{8}$$

By expressing the observed displacement in the Fourier domain, different plane wave contributions, or, in other words, different angle-of-arrival, can be identified. For this purpose, the frequency axis is mapped into the k_y axis [27]

$$k_y = (k_1^2 - k_x^2)^{1/2} \tag{9}$$

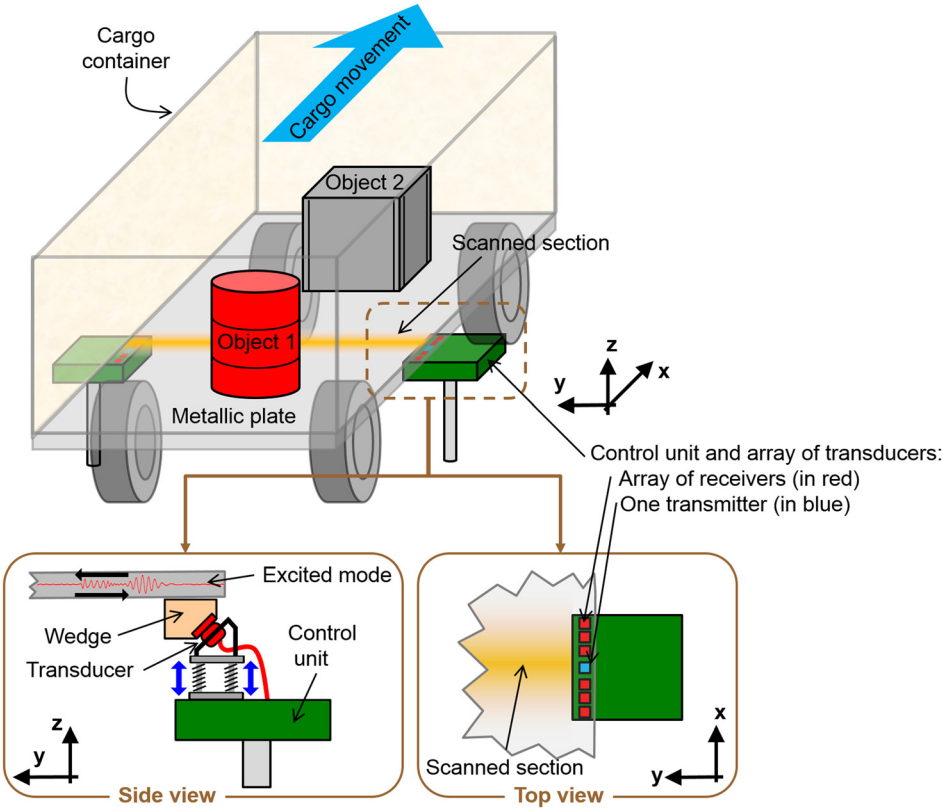

Fig. 2 General layout for ultrasound imaging applied to cargo inspection. Ultrasonic units are placed at inspected cargo sides, each formed by one transmitter and an array of receivers. Ultrasound images are created as the cargo moves across the scanning point. The whole ultrasonic image of the base plate is created by combining images retrieved at every cargo position.

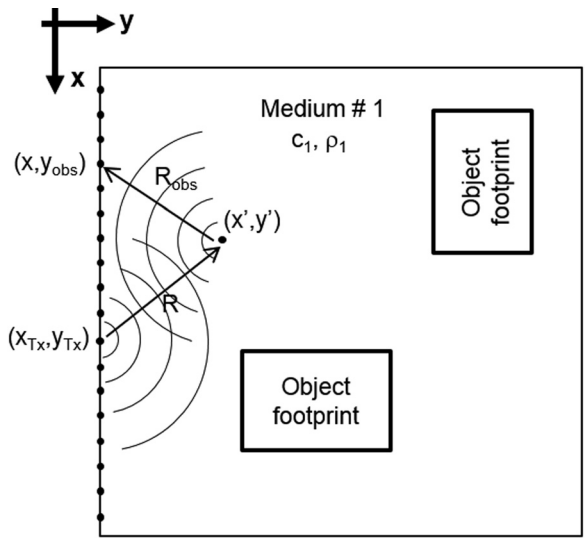

Fig. 3 Ultrasound imaging setup for detecting the footprint of objects place on a metallic plate. A point sourcelike transmitter is placed at (x_{Tx}, y_{Tx}). Receiving sensors are located at (x, y_{obs}). (x', y') is the point where the reflectivity is evaluated.

Thus, the plane wave spectrum of the observed displacement can be represented in the k_x-, k_y-domain, identifying the angle-of-arrival of the different plane wave components, as shown in Fig. 4.

Reflections in waveguide limits can be identified with those plane wave components with large angle-of-arrival values. In a limit case, filtering out all the plane wave components with angle-of-arrival greater than 0 deg would allow to identify the range position of all the objects within the waveguide, but at the expense of losing cross-range information. Thus, a tradeoff between range and cross-range information retrieval is set, by filtering out all the plane wave components with angle-of-arrival larger than α

$$U_{k,\text{filtered}}(y_{\text{obs}},k_y,k_x) = \{U_k(y_{\text{obs}},k_y,k_x) \text{ if } a\tan(k_y,k_x) < \alpha; 0 \text{ otherwise}\} \quad (10)$$

Finally, the filtered displacement in the Fourier domain is transformed back into the spatial x, y-domain

$$U_{\text{filtered}}(x,y_{\text{obs}},f) = \int_y U_{k,\text{filtered}}(y_{\text{obs}},k_y,k_x)\exp(+\mathbf{j}\,k_x x)dx \quad (11)$$

Ultrasonic reflectivity can be recovered by applying Eq. (1). In this case, responses due to reflections in walls with angles larger than α will not appear in the recovered ultrasonic reflectivity image.

2.3 Scanning System Implementation. As depicted in Fig. 2, the scanning unit is formed by a control unit and an array of transceivers (one transmitter and several receivers) that moves along the metallic base plate of the inspected cargo. A second scanning unit can be placed at the opposite side of the cargo in order to increase the accuracy of the scanning system.

The operation mode is as follows: first, at every position, the array of transceivers is attached to the metallic base plate. Next,

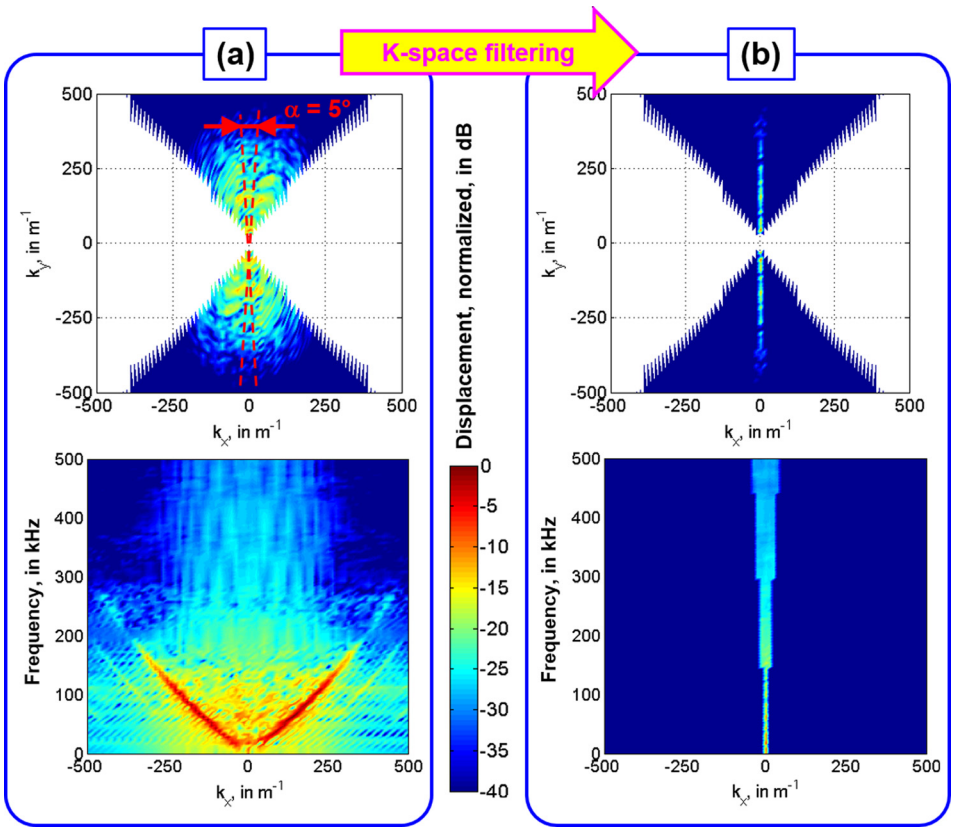

Fig. 4 Observed displacement representation in the Fourier domain. (*a*) Before filtering: dashed lines represent the limits of the filtered domain, defined by angle $\alpha = \pm 5$ deg. (*b*) After filtering. Both k_x, k_y space (upper row of plots) and k_x-frequency (lower row) representations are depicted.

the transmitter excites a guided wave, and receivers record the reflected waves. After that, the array of transceivers is detached from the plate, and moved to the next section of the metallic base plate to be scanned. Finally, the ultrasound responses of every scanned section are processed and plotted together, resulting in a single ultrasonic image of the metallic base plate.

Although the ultrasound-based scanning system has not been implemented yet, preliminary studies concerning the choice of the ultrasonic transducer technology that fits best the proposed system have been conducted.

The preferred solution is based on angle beam transducers (represented in Fig. 2), suitable for ultrasonic inspections with surface waves, where the excited Lamb mode can be controlled by the angle of the wedge [28,29]. The choice of a contact method is supported by the low cost of the transducers and the better dynamic range with respect to contactless solutions.

Electromagnetic acoustic transducers (EMAT) [13], whose scope of application is mainly restricted to electrically conduction objects (and thus metallic plates), have been considered as the best choice in case contactless sensors were needed, e.g., for the inspection of nonpolished metallic base plates that might damage contact transceivers. EMATs exhibit higher dynamic range than air-coupled transducers [30], although low noise amplifiers are likely to be required for signal amplification, thus increasing the complexity of the array of transceivers. Previous researches have successfully proved the capability of EMATs for Lamb wave modes excitation [31,32].

The placement of transmitting and receiving transducers also plays a key role in the design of the scanning system. This issue will be analyzed in Sec. 3.1, comparing several transmitting and receiving layouts, discussing the advantages and disadvantages of each.

3 Validation Examples

Three simulation-based examples are shown in Secs. 3.1, 3.2, and 3.3, each consisting of a more complex and realistic scenario than the predecessor. The forward ultrasonic problem is simulated using a 3D finite element method (FEM) [33]. Due to the moderate computational cost associated to FEM codes (both time and memory), and the limited computational resources (conventional laptop with 4 GB RAM and Intel® Core™ i5 Quad-core central processing unit at 2.67 GHz) available for testing the proposed scenarios, a smaller version of the realistic scenarios (overall dimension smaller than 1 m) is considered.

Nonetheless, thicknesses of the metallic and nonmetallic plates are the same as in a full-size problem, so the proposed modal analysis and imaging methodology can be straightforwardly used in simulated or measured data from large scattering problems. Additionally, the proposed un-optimized imaging algorithm can be used in real-time applications since calculation time is less than 5 s in the aforementioned conventional laptop.

First, the example described on page 8 of Ref. [34] (4 mm thick and 200 mm long steel plate, with Young's modulus $E = 205$ GPa, Poisson's ratio $\nu = 0.30$ and density $\rho = 7800\,\text{kg/m}^3$) has been simulated, in order to validate the selected software [33]. Phase velocity curves, group velocity curves, and Lamb wave modes have been calculated from simulation-based displacement results. Results representation fit those depicted in Figs. 1, 2, and 12 of Ref. [34], respectively, thus confirming that the proposed model developed with the commercial software [33] can be considered valid.

3.1 Single Metallic Plate With a Box on It. The first example consists of a single 1-cm-thick steel metallic plate with a box

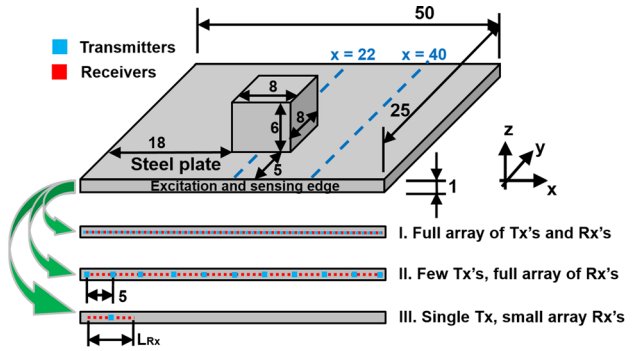

Fig. 5 Setup for the first simulation example. Several transmitting and receiving layouts (numbered from I–III) are considered. Units in cm.

on it, as shown in Fig. 5. The simulation parameters for steel are the following: P-wave velocity 5960 m/s, S-wave velocity 3220 m/s, and density 8000 kg/m^3.

Several excitation and recorded displacement layouts are considered, as shown in Fig. 5. The first one (layout I) consists of a full array of transmitters and receivers placed along the $y_{obs} = 0$ m side of the plate. Separation between array elements is 1 cm, thus yielding 50 transmitters and 50 receivers. This cross-range (x-axis) sampling rate is taken to avoid spatial aliasing, which is proportional to the separation between array elements. In layout I, all the elements will transmit at the same time, thus creating a plane wave that propagates toward the y (range) axis. This configuration is equivalent to a phased array system where all the elements transmit with the same delay [35].

3.1.1 Lamb Wave Modes Analysis. First, an analysis of the excited Lamb wave modes is carried out. Concerning the imaging application purpose, low-dispersive modes are required, thus setting a tradeoff between the use of high frequencies where dispersive modes are created, and lower frequencies that provide poorer imaging resolution. Recorded time-cross range displacement along $x = 40$ cm and $x = 22$ cm lines and the corresponding transformed response in the frequency–wavenumber domain are plotted in Figs. 6 and 7, respectively. Data processing for Lamb wave modes calculation that follows the procedure described in Ref. [34], consisting of the 2D Fourier Transform of the recorded displacement. For a better visualization of the excited Lamb wave modes, responses in the frequency–wavenumber domain from $x - \Delta x$ to $x + \Delta x$, with $\Delta x = 2$ cm, have been combined.

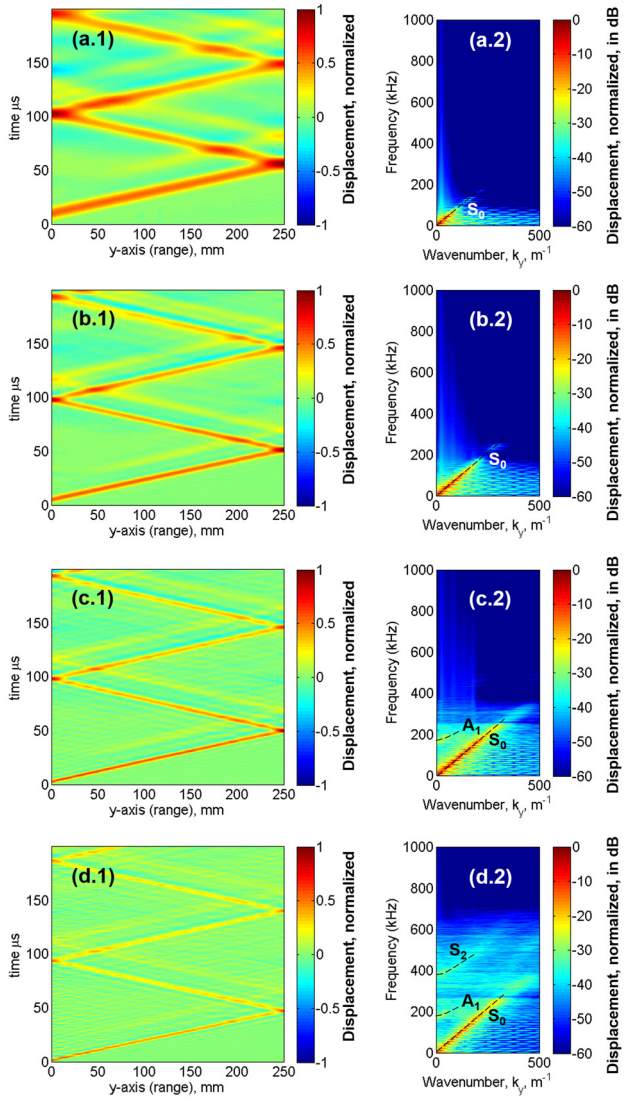

Fig. 6 Time-range ((*a*1)–(*d*1)) and frequency–wavenumber responses ((*a*2)–(*d*2)) recorded at $x = 40$ cm. Excitation tone burst: (*a*) 50 kHz, (*b*) 100 kHz, (*c*) 200 kHz, and (*d*) 400 kHz.

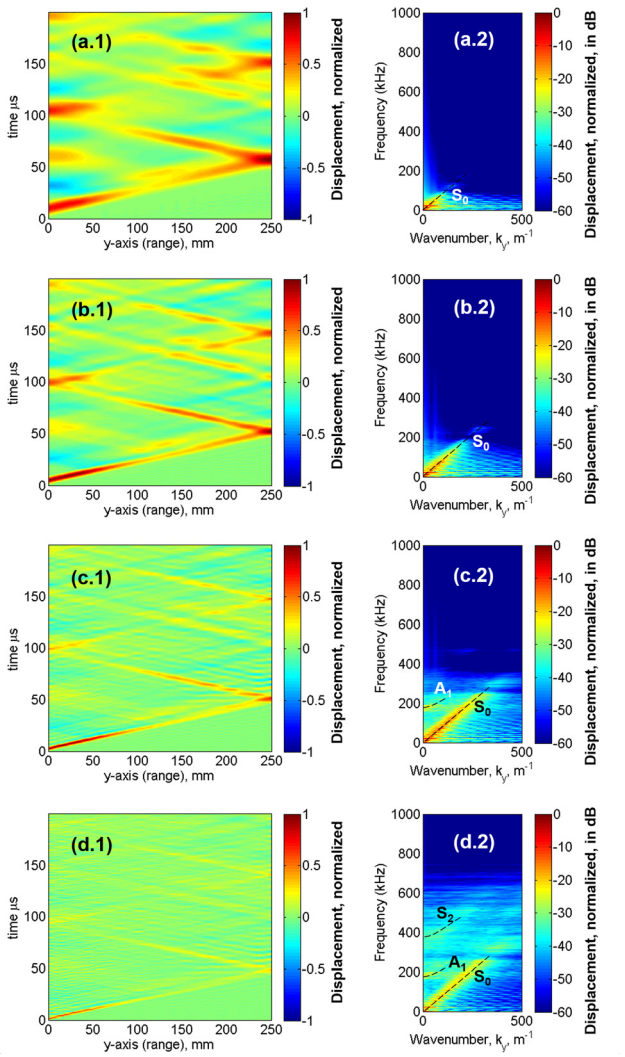

Fig. 7 Time-range ((*a*1)–(*d*1)) and frequency–wavenumber responses ((*a*1)–(*d*1)) recorded at $x = 22$ cm. Excitation tone burst: (*a*) 50 kHz, (*b*) 100 kHz, (*c*) 200 kHz, and (*d*) 400 kHz.

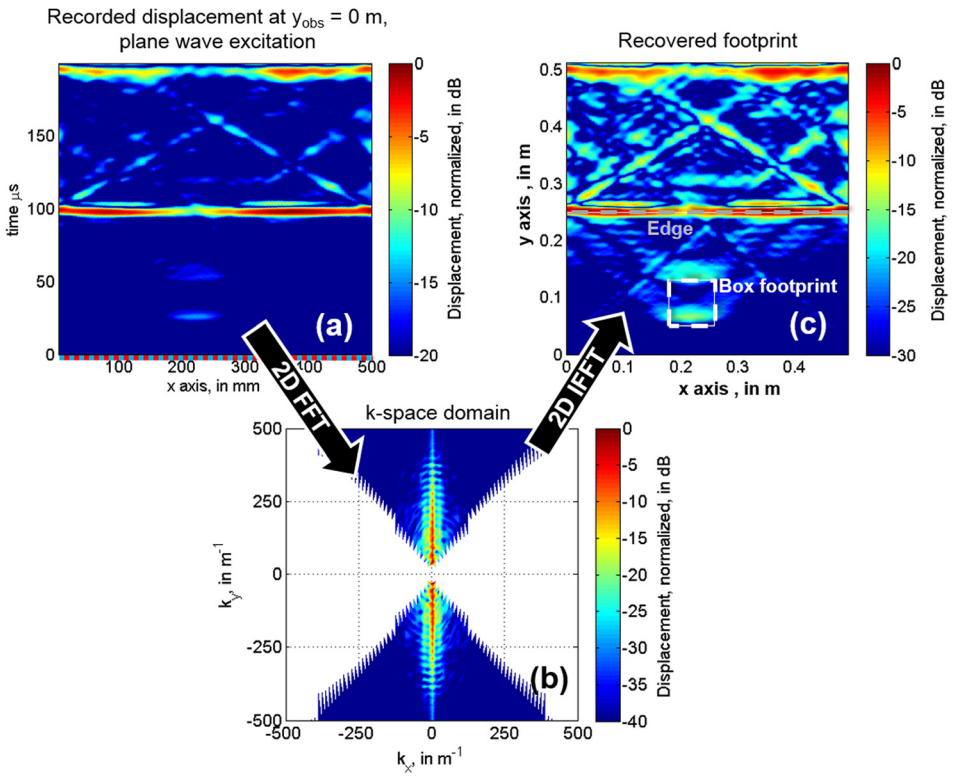

Fig. 8 Layout I, (*a*) recorded displacement along $y_{obs} = 0$ m line: time-cross range response. (*b*) Displacement in the *k*-space domain. (*c*) Backpropagated displacement in the imaging domain.

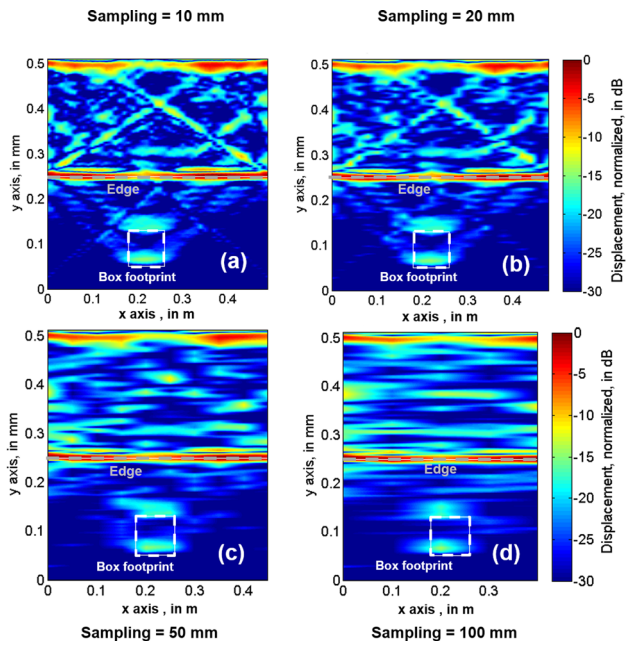

Fig. 9 Layout I, recovered displacement as a function of the separation between receiving array elements, Δx. (*a*) $\Delta x = 1$ cm, (*b*) $\Delta x = 2$ cm, (*c*) $\Delta x = 5$ cm, and (*d*) $\Delta x = 10$ cm.

A windowed tone burst is chosen as the excitation signal. The length of the rectangular window is equal to one period of the tone. Center frequencies from 50 kHz to 400 kHz were considered. The excitation signal bandwidth is 100% with respect to the tone frequency (e.g., from 25 to 75 kHz for the 50 kHz windowed tone burst). These excitation signals are chosen as a tradeoff between dispersion and range resolution. Larger bandwidth improves range resolution, but at the expense of increasing dispersion. Time axis is sampled every $\Delta t = 1$ μs, recording the displacement from $t_1 = 0$ μs to $t_2 = 200$ μs.

Either when considering the x-cut without ($x = 40$ cm, Fig. 6) or with the metallic box on top of the plate ($x = 22$ cm, Fig. 7), it is observed that only the S_0 mode is present up to 100 kHz. For higher excitation frequencies (400 kHz), S_0, A_1, and S_2 modes are excited. Thus, in order to avoid significant dispersion that degrades imaging results, a 100 kHz excitation tone is considered in further examples.

3.1.2 Layout I Imaging Results. Once the frequency of the excitation tone is chosen, imaging results for transmitting and receiving configuration layout I are retrieved. In this case, the receivers record the displacement along $y = 0$ m line. The time-cross range response is plotted in Fig. 8(*a*), where the reflections happening at the $y = 25$ cm edge as well as the front and rear metallic plate–box interfaces are clearly visible. Note that also the second reflection is also noticeable. After the first reflection, edge plate modes distort the backpropagated displacement (X-shape features observed in Fig. 8(*a*)).

It must be indicated that the reflection happening at the edge of the plate ($y = 25$ cm for this example) opposed to the transmitter can be used together with the apriori knowledge of the plate width to recover an accurate estimation of the excited Lamb mode velocity, c_1. As the distance at which the opposite edge reflection happens is known (that is, the plate width), it is possible to calculate the c_1 value to set this reflection in place ($c_1 = 5100$ m/s for this example).

The recorded displacement is transformed into the *k*-space by taking the fast Fourier transform across time and cross-range (x-) axis (Eqs. (6) and (7)). The plane wave spectrum is plotted in Fig. 8(*b*). As the array of transmitters creates a plane wavefront, most of the wavemodes correspond to normal direction of arrival. Finally, the wavemodes are transformed back in the

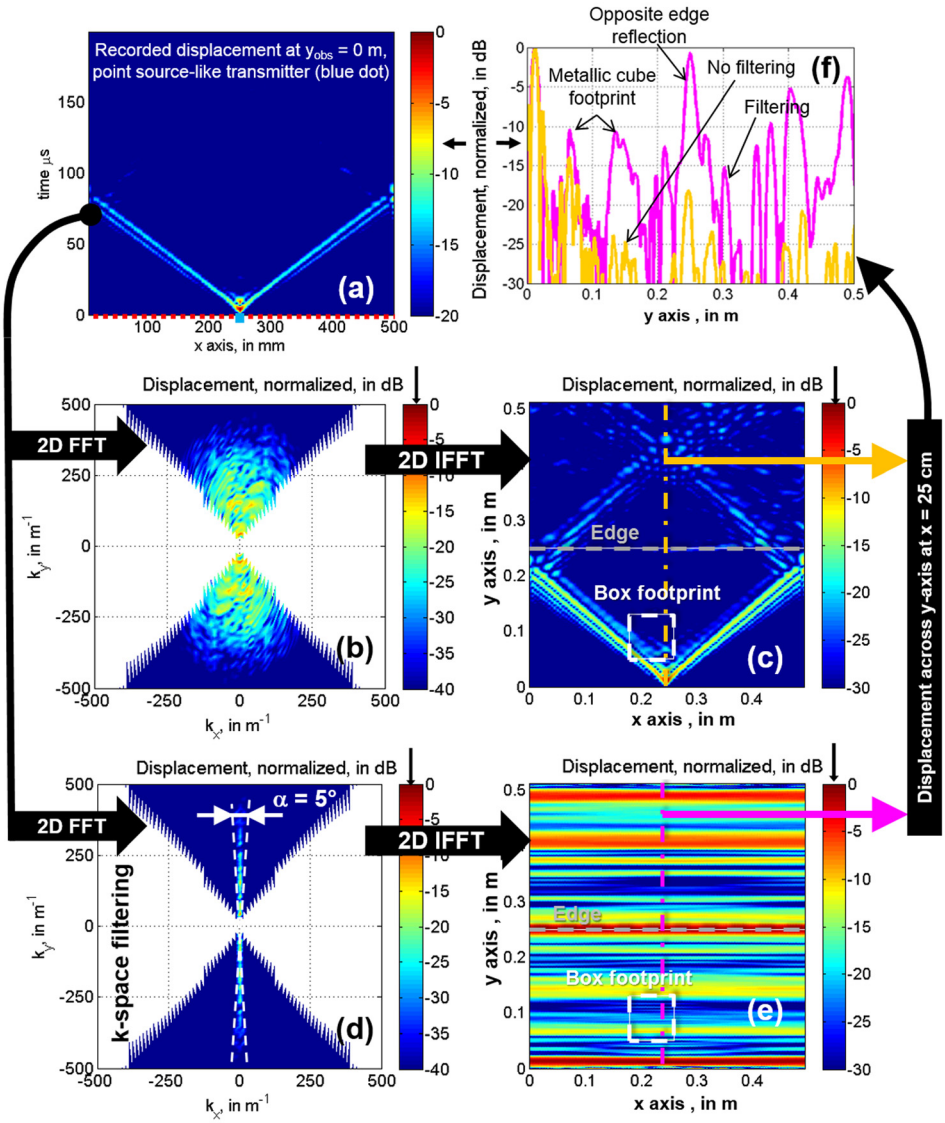

Fig. 10 Layout II, single transmitter placed at $x_{Tx} = 25$ cm. (*a*) Recorded displacement along $y_{obs} = 0$ m line: time-cross range response. (*b*) Displacement in the *k*-space domain. (*c*) Backpropagated displacement in the imaging domain. (*d*) Displacement in the *k*-space domain after filtering with $\alpha = 5$ deg. (*e*) Backpropagated displacement in the imaging domain after filtering with $\alpha = 5$ deg. (*f*) Comparison of the nonfiltered and filtered displacements for $x = 25$ cm.

range-cross-range imaging domain, yielding the footprint image depicted in Fig. 8(*c*). The backpropagated displacement matches the true footprint of the considered layout.

As mentioned before, separation between sensors in the cross-range (x-) axis, Δx, has to be chosen to prevent aliasing. Recovered images for different Δx values ranging from 1 cm to 10 cm are depicted in Fig. 9. Spatial aliasing degrades cross-range image resolution for higher Δx values.

3.1.3 Layout II Imaging Results. For the considered arrangement of transmitters and receivers (layout I), *k*-space domain filtering does not have a significant impact in the improvement of the image quality as most of the wavemodes are in the $k_x = 0$ axis. The effectiveness of *k*-space filtering is shown in layout II, consisting of a single transmitter and a full array of receivers. The number of receiving elements is again 50, with $\Delta x = 1$ cm spacing. A point sourcelike transmitter is considered, creating a cylindrical pressure wave.

Figure 10(*a*) shows the recorded time-cross range displacement for a single transmitter placed at $x_{Tx} = 25$ cm (with x_{Tx} the position of the transmitter). Note that the excitation corresponds to a cylindrical wave, as opposed to layout I, which was a plane wave. Then, the *k*-space response (Fig. 10(*b*)) shows plane wave components propagating in all the possible traveling directions (filling the *k*-space domain), as expected for a cylindrical wave. The backpropagated displacement shows up neither the footprint of the box nor the plate edge at $y = 25$ cm, but the wavefront of the cylindrical wave (Fig. 10(*c*)).

To remove nondesired cylindrical wave components, *k*-space filtering can be applied with small α-angle (e.g., $\alpha = 5$ deg). Filtered *k*-space domain is plotted in Fig. 10(*d*), where only components with $k_x \ll k_y$ are left. That is, only those plane waves traveling in the y-axis are considered. The backpropagated displacement of the filtered wavemodes is depicted in Fig. 10(*e*), where the reflections happening at $y = 25$ cm and on the front and rear plate–box interfaces are visible. The price to pay is a loss of cross-range resolution: for an α angle close to 0 deg, only the backpropagated displacement across $x = x_{Tx} = 25$ cm is recovered. This response is replicated throughout the entire cross-range (i.e., for every x-axis value). Finally, for the sake of clarity, the displacement across y-axis for $x = 25$ cm is depicted in Fig. 10(*f*), comparing the results before and after *k*-space filtering.

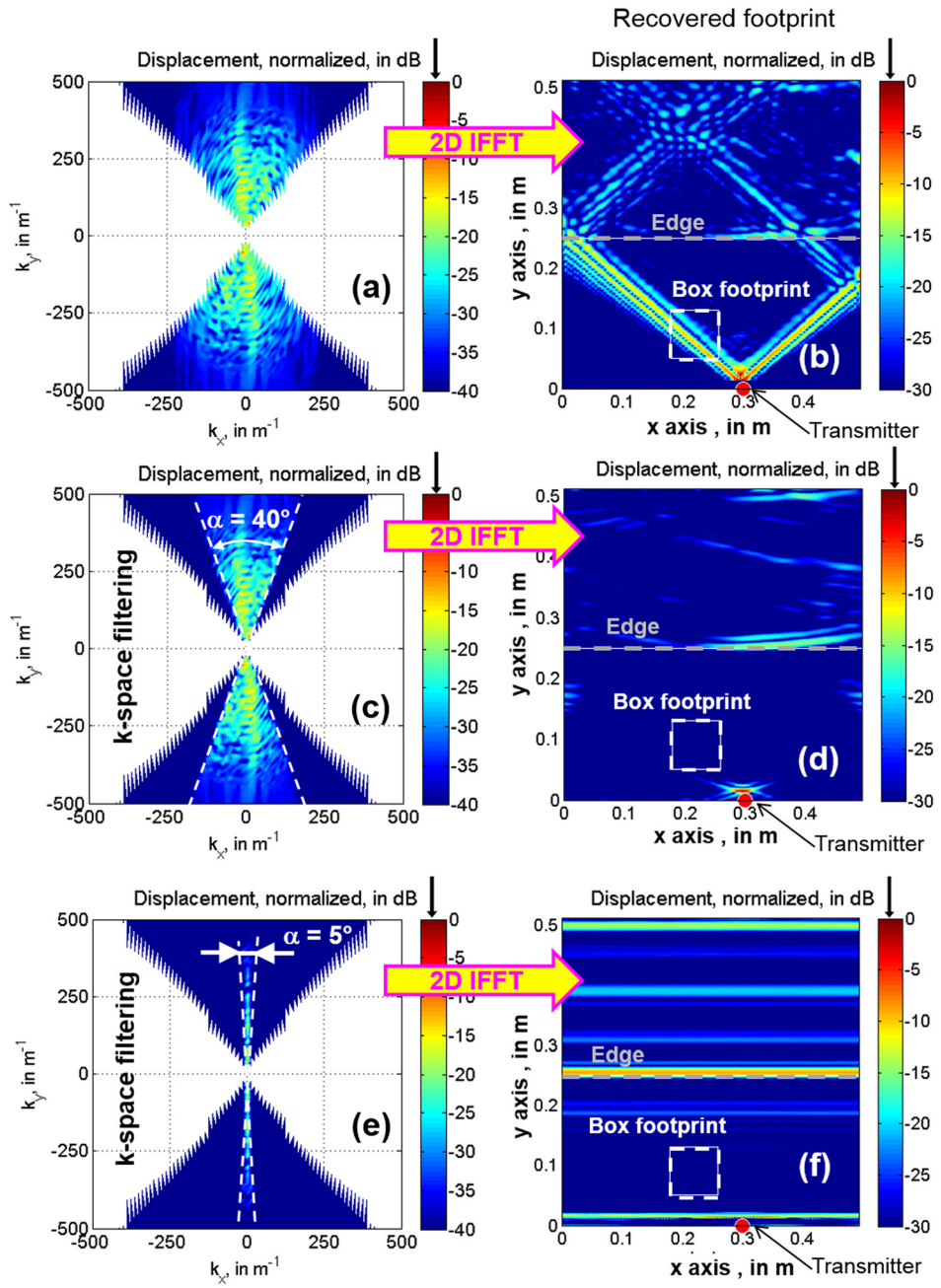

Fig. 11 Layout II, single transmitter placed at $x_{Tx} = 30$ cm. Comparison for different filtering angles α: ((*a*) and (*b*)) no filtering. ((*c*) and (*d*)) Filtering angle $\alpha = 40$ deg. ((*e*) and (*f*)) Filtering angle $\alpha = 5$ deg. Left column plots represent the displacement in the *k*-space after filtering. Right column plots represent the backpropagated displacement in the imaging domain.

The concept of *k*-space filtering is also illustrated in Fig. 11, where the filtered displacement in the *k*-space (left column plots) and the backpropagated image (right column plots) is depicted for different α angles. In this case, the point sourcelike transmitter is placed at $x_{Tx} = 30$ cm. For $\alpha = 40$ deg, the reflection at $y = 25$ cm is slightly noticeable, as well as the reflection of the transmitted cylindrical wave on the lateral sides of the metallic plate (located at $x = 0$ and 50 cm, $y = 15$ cm).

It is possible to increase the cross-range imaging resolution by placing more transmitters in the $y = 0$ axis, as depicted in Fig. 5, layout II. The same *k*-space filtering as explained before is carried out for the recorded displacement for every transmitter. Moreover, an additional cross-range mask with $L = 5$ cm width, centered on every transmitter, is applied. Imaging results are depicted in Fig. 12 for all the 11 considered transmitters. Note that for every $L = 5$ cm section, the image remains constant across *x*-direction. Increasing the number of transmitters will lead to the same image as in Fig. 8(*c*).

3.1.4 Layout III Imaging Results. Practical implementation of the ultrasound imaging system using the transmitting and receiving layout II supposes an advantage with respect to layout I as the number of transmitters is reduced from 50 to 11, although the number of receivers is still high: 50 receivers evenly spaced in the 50 cm length edge are used.

This issue is studied with the transmitting and receiving arrangement presented in layout III, consisting of a single transmitter and an array of receivers of length L_{Rx}. Separation between

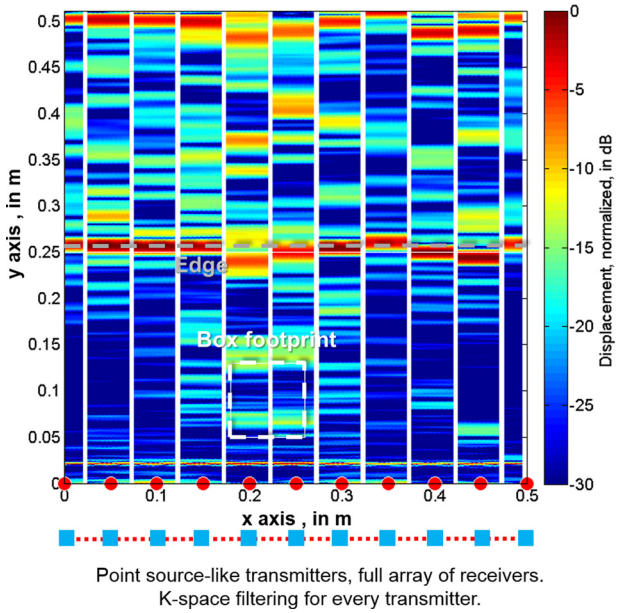

Fig. 12 Layout II, multiple transmitters evenly spaced every 5 cm in the $y = 0$ axis. Imaging results for every transmitter are masked with $L = 5$ cm width mask centered on the corresponding transmitter.

receiving elements is again 1 cm. The transmitter and the receiving array are displaced in 5-cm step along the $x = 0$ side of the plate, then applying the same cross-range mask as for imaging results with layout II. In practice, this is equivalent to the configuration depicted in Fig. 2, where the ultrasound sensor would be static while the cargo moves through the scanning facility allowing the imaging of the metallic base plate.

For layout III, the parameter to be swept is L_{Rx}. Imaging results for $L_{Rx} = 10$ cm, 20 cm, and 40 cm are depicted in Figs. 13(a)–13(*c*), respectively. For every case, the number of receiving elements is 10, 20, and 40. As expected, cross-range resolution is reduced for smaller receiving arrays (Fig. 13(*a*)). A $L_{Rx} = 40$ cm receiving array yields similar resolution as the full receiving array of layout II.

Thus, practical implementation of the scanning system depicted in Fig. 2 would be feasible using a single transmitting transducer, and an array of 40 receiving transducers, resulting in a simpler setup with respect to the use of a full array of transmitting and receiving transducers (layout I).

3.1.5 Phased Array Analysis. Layouts I, II, and III can be studied from the point-of-view of phased array theory. As described in Ref. [35], there are two main kinds of approaches for imaging systems: conventional full phased array (FPA) imaging that produces the best image quality by using all elements for both transmission and reception, and classical synthetic aperture (CSA) imaging, with one transmitter or receiver element at the same time. FPA requires complex hardware to synchronize transmission and reception, whereas CSA image is created by coherently combining the images for multiple positions, thus simplifying hardware complexity.

An idea of the effective aperture is given by the convolution of the transmit and receive aperture functions, and is denoted coarray [35]. Figure 14 shows the comatrix representation (in this matrix, each transmit/receive element pair contributes to a specific bin of the coarray [35]) and the resulting coarray functions. For illustration purposes, arrays of eight elements are considered. Layout I, which corresponds to an FPA, produces the highest coarray function, thus resulting in the highest image resolution. If one out of five transmitting elements are considered (layout II), sparse transmitting array, the resulting coarray function is flattened, resulting

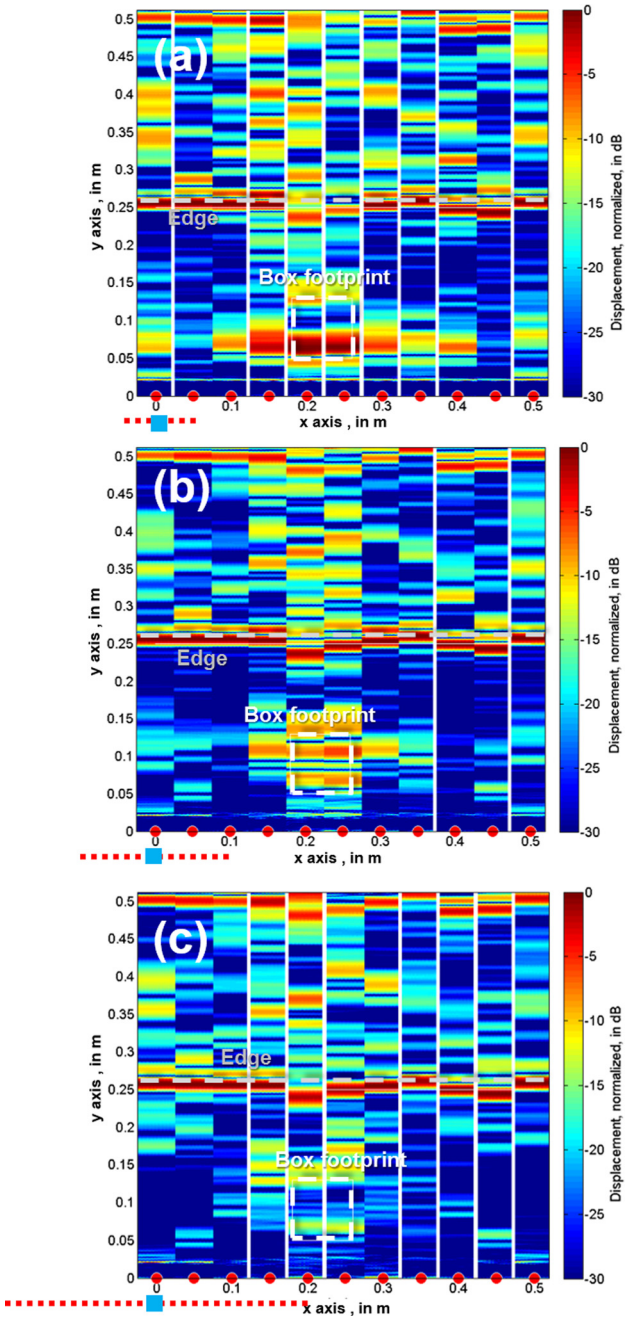

Fig. 13 Imaging results for layout III, receiving array of length L_{Rx}, with a point transmitter placed in the center. The transmitter and the receiving array are displaced in 5 cm-steps. (*a*) $L_{Rx} = 10$ cm, (*b*) $L_{Rx} = 20$ cm, and (*c*) $L_{Rx} = 40$ cm.

in loss of resolution (Fig. 12). Finally, layout III exhibits a narrower coarray function, reducing even more the resolution. To overcome this issue, layout III setup is moved to create a synthetic aperture (Fig. 13), as proposed in the scanning system architecture depicted in Fig. 2.

3.1.6 Detection Capabilities Analysis. Once the effectiveness of the *k*-space filtering has been validated, attention will be put back on the imaging capabilities for the detection of metallic containers on cargo. For the sake of clarity, the transmitting and receiving layout I (full array of transmitters and receivers) is considered again.

Figure 15 represents the imaging results for four different situations: Fig. 15(*a*) corresponds to the case in which nothing is

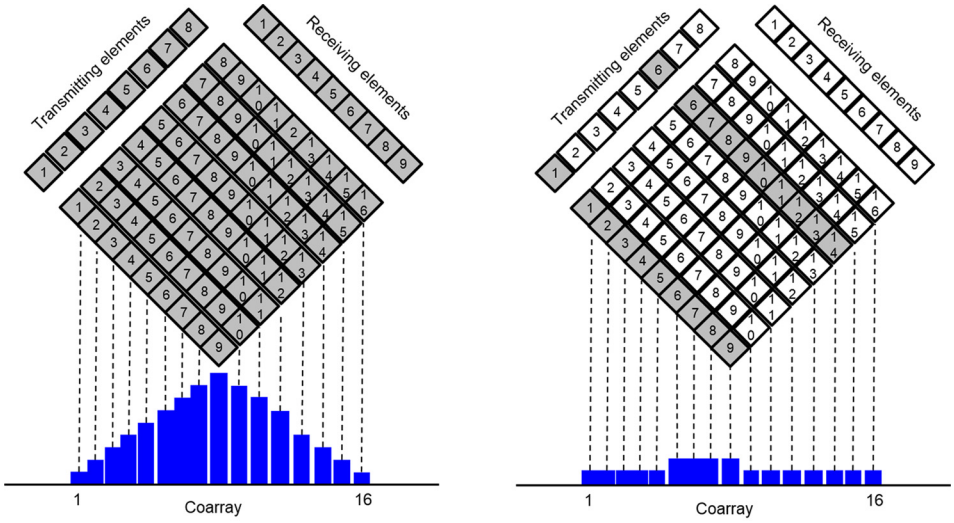

Layout I: Conventional full phased array

Layout II: Sparse transmitters.

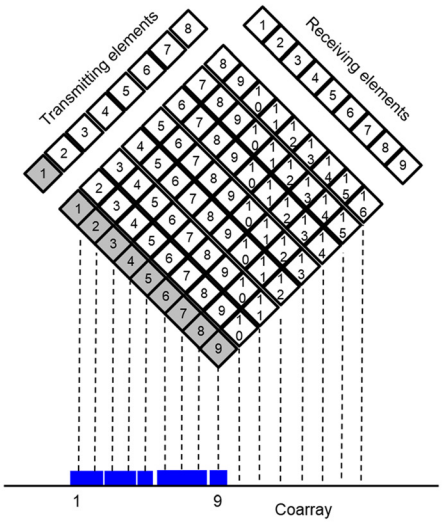

Layout III: Single transmitter, full array of receivers

Fig. 14 Phased array analysis of layouts I, II, and III. Comatrix and coarray representation [35]. Co array is an indicator of the effective aperture of the system.

placed on top of the metallic plate. The only noticeable artifacts are the first and second reflections on the $x = 25$ cm edge, as well as the X-shape waveforms created by edge modes. Figure 15(*b*) shows the footprint when a wooden box (density 1200 kg/m^3), having the same dimensions and placed at the same position as the metallic box in Fig. 5, is considered. The reflections in the steel-wood interface are hardly noticeable. Next, a box made of aluminum (density 2700 kg/m^3, S-wave velocity 3100 m/s, P-wave velocity 6320 m/s) is considered. Imaging results are depicted in Fig. 15(*c*) where the aluminum box footprint becomes more noticeable than the wooden box. Finally, Fig. 15(*d*) corresponds to a box made of lead, a high *Z*-number material. Although the footprint is less intense than steel (Fig. 9(*a*)), it can be detected. To complement Fig. 15 results, Table 1 summarizes the mechanical characteristics and the acoustic impedance of the tested materials. Note that aluminum ($Z = 13$) and lead ($Z = 82$) have similar acoustic impedance, so it could be expected that they create footprints with similar intensities (Figs. 15(*c*) and 15(*d*)).

As a conclusion, the footprint of containers made of materials with similar characteristics as the guided medium (in this case, a metallic steel plate) will show up. This fact is of interest in the case of compartments camouflaged in the cargo structure as illustrated in Fig. 1.

3.2 Closed Metallic Container With a Box in It. In the second example, the complexity of the geometry is increased by considering a closed metallic container with 1-cm thick walls. This kind of structure requires high energy radiation (e.g., X-ray) to be capable of penetrating the metallic walls for nondestructive testing (NDT). Thus, the interest of this example is to prove the capability of ultrasound imaging to detect a metallic object on the floor of a scaled metallic cargo container. The proposed setup is plotted in Fig. 16. For the sake of clarity, the transmitting and receiving layout I (see Fig. 5) is considered.

Imaging results are plotted in Fig. 17. Clearly, the reflection at the back side of the metallic container is again noticeable (happening at $x = 25$ cm), as well as the reflections on the metallic box–container floor front and rear interfaces.

3.3 Closed Metallic Container With Assets of Different Kind in It. The third example aims to resemble an even more realistic scenario by considering the same closed metallic container

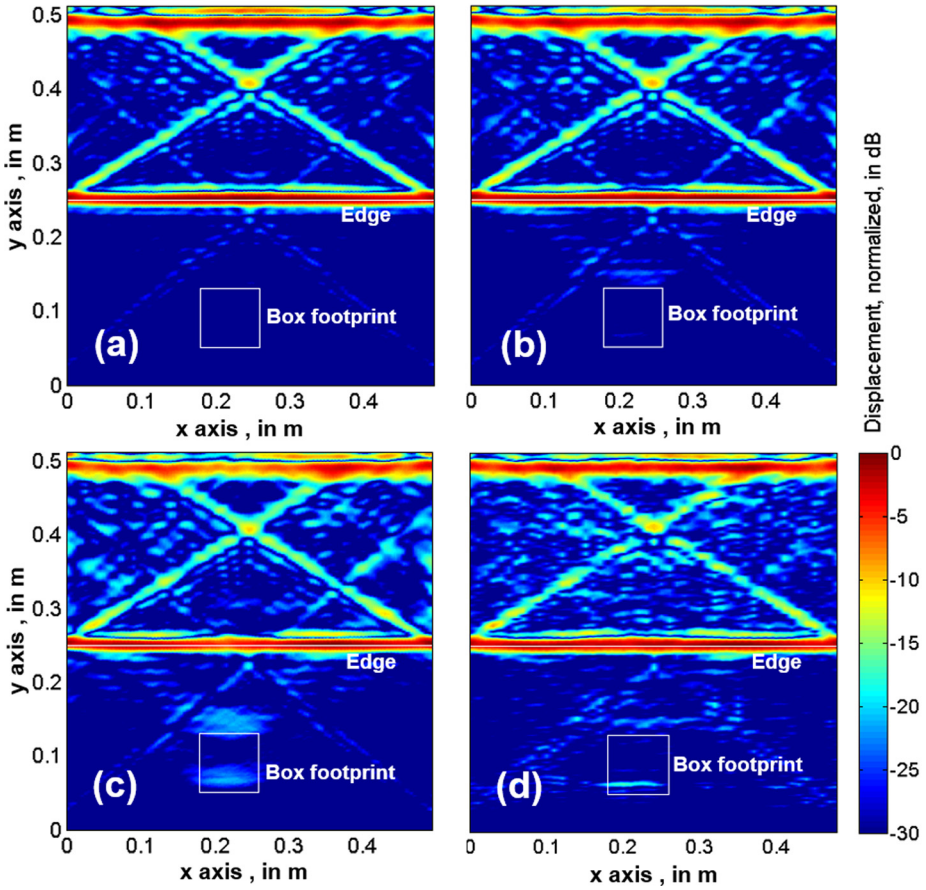

Fig. 15 Imaging results for: (*a*) no box on top of the steel plate, (*b*) wooden box, (*c*) aluminum box, and (*d*) lead box. Transmitting and receiving layout I is considered.

Table 1 Mechanical properties and acoustic impedance of the tested materials

Material	Z number	Density (kg/m^3)	P-wave velocity (m/s)	S-wave velocity (m/s)	Wave velocity (m/s)	Poisson's ratio	Acoustic impedance (MPa s/m^3)
Wood		1200	4200	3300	2240	0.34	2.02
Aluminum	13	2700	6320	3100	5100	0.35	13.77
Iron	26	7870	5960	3220	5200	0.29	40.92
Steel		8000	5960	3220	5000	0.29	40.00
Lead	82	11,400	1960	700	1210	0.44	13.79

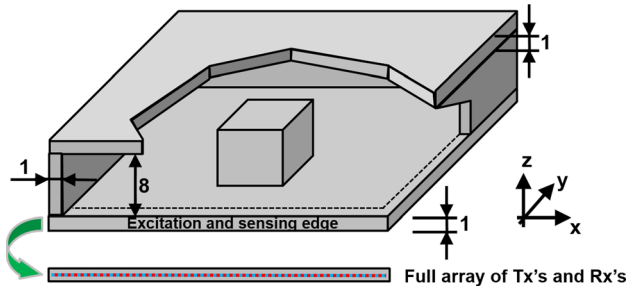

Fig. 16 Setup for the second simulation example. Transmitting and receiving layout I is considered (units in cm).

as in the second example, but now with assets of different size, shape, and composition in it. The goal is to show that only the footprint of metallic objects is detected. The geometry model is plotted in Fig. 18: plastic (one containing water), wooden, and metallic containers are considered.

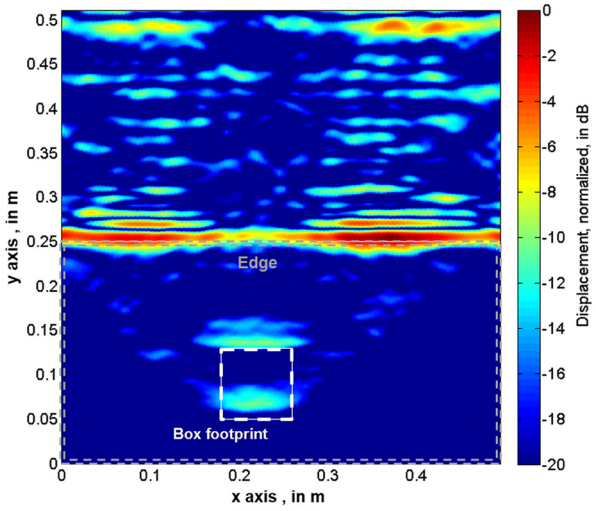

Fig. 17 Imaging results for the second simulation example (setup depicted in Fig. 16) consisting of a closed metallic container with a metallic box in it

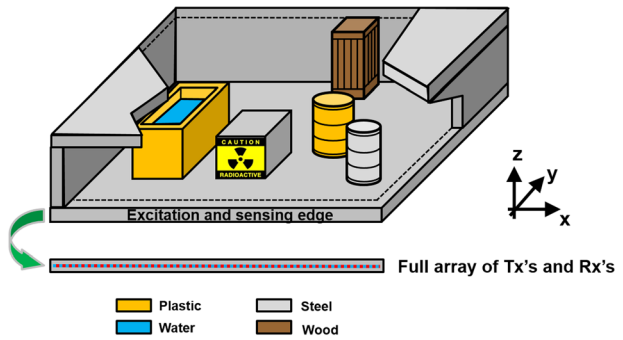

Fig. 18 Setup for the third simulation example. Transmitting and receiving layout I is considered. Colors indicate the composition of each asset.

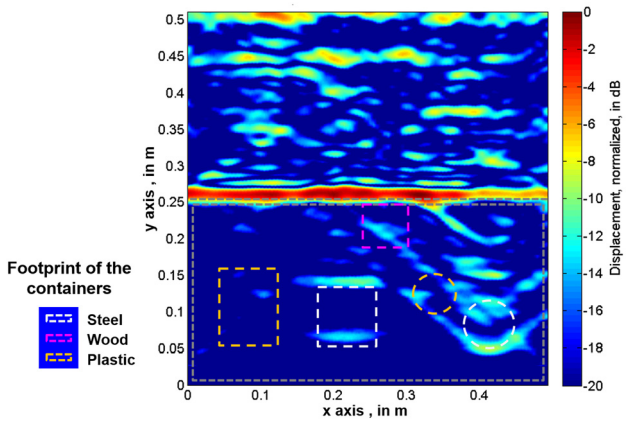

Fig. 19 Imaging results for the third simulation example (setup depicted in Fig. 18) consisting of a closed metallic container with several assets in it. Solid lines indicate the true footprint and the material of each asset.

Figure 19 shows the imaged footprint for this third example. Only steel-made assets footprint is recovered. Note that in the case of the cylindrical metallic object, the tails are more noticeable than the ones for the cubic metallic container (the one marked with a "radiation hazard" warning sign in Fig. 18).

4 Conclusions

The set of simulation-based results have demonstrated the feasibility of using ultrasound guided wave imaging for inspecting cargo containers in real-time applications. Variations in the constitutive properties or thickness on the metallic floor of a cargo container create reflections that can be identified by the proposed imaging algorithm, thus revealing the location of the objects or concealed compartments inside the container. In particular, the imaging algorithm has been tested in a realistic scenario, consisting of a closed metallic container with several assets of different kinds inside of it. Not only the proposed ultrasound-based imaging methodology is capable of creating a footprint of the concealed metallic object but also it is not cluttered by other nonmetallic, low Z number structures. Location of the metallic objects is given with an uncertainty smaller than 4–5 cm for a 50×25 cm scenario size. The proposed Fourier-based imaging technique has proved to be an easy and effective way to get rid of reflections in guided medium bounds and to generate real-time images. Further work is devoted to test the proposed methodology with measurements.

In summary, the proposed methodology presents a new paradigm on how to detect metallic containers on cargo, which can be used for shielding nuclear threats, by identifying their metallic footprint on the cargo metallic base plate. This methodology also has the potential to enhance the efficacy of high-energy NDT methods, such as X-ray inspection systems, traditionally used in similar applications.

Acknowledgment

This work has been partially supported by the "Universidad de Oviedo" under International Campus of Excellence (CEI) mobility grants (2012–2013). This material is based upon the work supported by the U.S. Department of Homeland Security (DHS), Science and Technology Directorate, Office of University Programs, under Grant Award 2013-ST-061-ED0001. The authors would like to acknowledge Mr. Ashkan Ghanbarzade for their help in 3D FEM simulations.

References

[1] Medalia, J., 2010, *Detection of Nuclear Weapons and Materials: Science, Technologies, Observations*, DIANE Publishing, Collingdale, PA.
[2] Chang, C. L., He, M., and Nguyen, M. H., 2010, "Computational Model for Automatic Cargo Container Inspection Systems," IEEE International Conference on Technologies for Homeland Security (HST), Waltham, MA, Nov. 8–10, pp. 556–561.
[3] European Commission—Customs 2002, "Chapter 3—Container Specifications," *Good Practice Guide*.
[4] Rock-It Cargo, 2009, "Air Container Specifications," Rock-It Cargo, London, accessed Nov. 25, 2015, http://www.rockitcargo.com/uploads/AirContainerSpecs.pdf
[5] Avramides, A., and Henstock, P., 1995, "Air Cargo Containers," U.S. Patent No. 5,398,831.
[6] Hall, J. S., Fromme, P., and Michaels, J. E., 2011, "Ultrasonic Guided Wave Imaging for Damage Characterization," 2011 Aircraft Airworthiness and Sustainment Conference (AA&S), San Diego, CA, Apr. 17–21.
[7] Michaels, J. E., 2008, "Detection, Localization and Characterization of Damage in Plates With an In Situ Array of Spatially Distributed Ultrasonic Sensors," Smart Mater. Struct., **17**(3), p. 035035.
[8] Ros, K., and Fink, M., 2001, "Ultrasonic Imaging Using Spatio-Temporal Matched Field (STMF) Processing—Applications to Liquid and Solid Waveguides," IEEE Trans. Ultrasonics, Ferroelectrics, Freq. Control, **48**(2), pp. 374–386.
[9] Martinez-Lorenzo, J. A., and Alvarez-Lopez, Y., 2014, "An Ultrasonic Approach for Sensing and Imaging Shielding Containers of Nuclear Threats," ASME Paper No. DSCC2014-6183.
[10] Knab, L. J., Blessing, G. V., and Clifton, J. R., 1983, "Laboratory Evaluation of Ultrasonics for Crack Detection in Concrete," Am. Concr. Inst. J. Proc., **80**(1), pp. 17–23.
[11] Cawley, P., 2003, "Practical Long Range Guided Wave Inspection—Applications to Pipes and Rail," Second Middle East Nondestructive Testing Conference and Exhibition, Jubai Industrial City, Saudi Arabia, Dec. 8–10.
[12] Mohr, W., and Holler, P., 1976, "On Inspection of Thin-Walled Tubes for Transverse and Longitudinal Flaws by Guided Ultrasonic Waves," IEEE Trans. Sonics Ultrasonics, **23**(5), pp. 369–373.
[13] Salzburger, H. J., Dobmann, G., and Mohrbacher, H., 2001, "Quality Control of Laser Welds of Tailored Blanks Using Guided Waves and EMATs," IEEE Proc. Sci. Meas. Technol., **148**(4), pp. 143–148.
[14] Rose, J. L., and Soley, L., 2000, "Ultrasonic Guided Waves for Anomaly Detection in Aircraft Components," Mater. Eval., **58**(9), pp. 1080–1086.
[15] Chang, F. H., Drake, T. E., Osterkamp, M. A., Prowant, R. S., Monchalin, J. P., Heon, R., Bouchard, P., Padioleau, C., Froom, D. A., Frazier, W., and Barton, J., 1993, "Laser Ultrasonic Inspection of Honeycomb Aircraft Structures," Review of Progress in Quantitative Nondestructive Evaluation, pp. 611–616.
[16] Ahuja, A. T., Griffith, J. F., Wong, K. T., Antonio, G. E., Chu, W. C., and Ho, S. S., 2007, *Diagnostic Imaging: Ultrasound*, 1st ed., AMIRSYS Publishing, Inc., Salt Lake City, UT.
[17] Rose, J. L., 1999, *Ultrasonic Waves in Solid Media*, Cambridge University Press, New York.
[18] Fromme, P., and Sayir, M. B., 2002, "Detection of Cracks at Rivet Holes Using Guided Waves," Ultrasonics, **40**(1), pp. 199–203.
[19] Guo, N., and Cawley, P., 1993, "The Interaction of Lamb Waves With Delaminations in Composite Laminates," J. Acoust. Soc. Am., **94**(4), pp. 2240–2246.
[20] Harley, J. B., and Moura, J. M. F., 2013, "Sparse Recovery of the Multimodal and Dispersive Characteristics of Lamb Waves," J. Acoust. Soc. Am., **133**(5), pp. 2732–2745.
[21] Harley, J. B., and Moura, J. M. F., 2014, "Data-Driven Matched Field Processing for Lamb Wave Structural Health Monitoring," J. Acoust. Soc. Am., **135**(3), pp. 1231–1244.
[22] Alleyne, D. N., and Cawley, P., 1992, "The Interaction of Lamb Waves With Defects," IEEE Trans. Ultrasonics, Ferroelectrics, Freq. Control, **39**(3), pp. 381–397.
[23] Eisenhardt, C., Jacobs, L. J., and Qu, J., 1999, "Application of Laser Ultrasonics to Develop Dispersion Curves for Elastic Plates," ASME J. Appl. Mech., **66**(4), pp. 1043–1045.

[24] Rogge, M. D., and Leckey, C. A., 2013, "Characterization of Impact Damage in Composite Laminates Using Guided Wavefield Imaging and Local Wavenumber Domain Analysis," Ultrasonics, **53**(7), pp. 1217–1226.
[25] Yu, L., Tian, Z., and Leckey, C. A., 2015, "Crack Imaging and Quantification in Aluminum Plates with Guided Wave Wavenumber Analysis Methods," Ultrasonics, **62**, pp. 203–212.
[26] Norton, S. J., and Linzer, M., 1981, "Ultrasonic Reflectivity Imaging in Three Dimensions: Exact Inverse Scattering Solutions for Plane, Cylindrical, and Spherical Apertures," IEEE Trans. Biomed. Eng., **28**(2), pp. 201–220.
[27] Mayer, K., Marklein, R., Langenberg, K. J., and Kreutter, T., 1990, "Three-Dimensional Imaging System Based on Fourier Transform Synthetic Aperture Focusing Technique," Ultrasonics, **28**(4), pp. 241–255.
[28] Ditri, J. J., and Rajana, K. M., 1995, "Analysis of the Wedge Method of Generating Guided Waves," *Review of Progress in Quantitative Nondestructive Evaluation*, Springer, New York, pp. 163–170.
[29] Luo, W., and Rose, J. L., 2004, "Lamb Wave Thickness Measurement Potential With Angle Beam and Normal Beam Excitation," Mater. Eval., **62**(8), pp. 860–866.
[30] Castaings, M., and Cawley, P., 1996, "The Generation, Propagation, and Detection of Lamb Waves in Plates Using Air-Coupled Ultrasonic Transducers," J. Acoust. Soc. Am., **100**(5), pp. 3070–3077.
[31] Guo, Z., Achenbach, J. D., and Krishnaswamy, S., 1997, "EMAT Generation and Laser Detection of Single Lamb Wave Modes," Ultrasonics, **35**(6), pp. 423–429.
[32] Dixon, S., Edwards, C., and Palmer, S. B., 2003, "The Optimization of Lamb and Rayleigh Wave Generation Using Wideband-Low-Frequency EMATs," Rev. Prog. Quant. Nondestructive Eval., **20**(A&B), pp. 297–304.
[33] COMSOL, 2016, "Comsol Multiphysics," Comsol Inc., Burlington, MA, accessed Sept. 5, 2015, www.comsol.com
[34] Hora, P., and Červená, O., 2012, "Determination of Lamb Wave Dispersion Curves by Means of Fourier Transform," Appl. Comput. Mech., **6**(1), pp. 5–16.
[35] Johnson, J. A., Karaman, M., and Khuri-Yakub, B. T., 2005, "Coherent-Array Imaging Using Phased Subarrays. Part I: Basic Principles," IEEE Trans. Ultrasonics, Ferroelectrics, Freq. Control, **52**(1), pp. 37–50.